Dartmouth College
Dartmouth Digital Commons

Open Dartmouth: Faculty Open Access Articles

11-21-2013

Spectral Energy Distributions of Type 1 AGN in XMM-COSMOS – II. Shape Evolution

Heng Hao
Harvard–Smithsonian Center for Astrophysics

Martin Elvis
Harvard–Smithsonian Center for Astrophysics

Francesca Civano
Dartmouth College

Gianni Zamorani
National Institute for Astrophysics (INAF)

Follow this and additional works at: https://digitalcommons.dartmouth.edu/facoa

Part of the External Galaxies Commons, and the Physical Processes Commons

Spectral energy distributions of type 1 AGN in *XMM*-COSMOS – II. Shape evolution

Heng Hao,[1,2]★ Martin Elvis,[2] Francesca Civano,[2,3] Gianni Zamorani,[4] Luis C. Ho,[5] Andrea Comastri,[4] Marcella Brusa,[6,7] Angela Bongiorno,[6,8] Andrea Merloni,[6] Jonathan R. Trump,[9] Mara Salvato,[10,11] Chris D. Impey,[12] Anton M. Koekemoer,[13] Giorgio Lanzuisi,[6] Annalisa Celotti,[1,14,15] Knud Jahnke,[16] Cristian Vignali,[4,7] John D. Silverman,[17] C. Megan Urry,[18] Kevin Schawinski[19] and Peter Capak[20]

[1]*SISSA, Via Bonomea 265, I-34136 Trieste, Italy*
[2]*Harvard–Smithsonian Center for Astrophysics, 60 Garden Street, Cambridge, MA 02138, USA*
[3]*Department of Physics and Astronomy, Dartmouth College, 6127 Wilder Lab, Hanover, NH 03755, USA*
[4]*INAF – Osservatorio Astronomico di Bologna, via Ranzani 1, I-40127 Bologna, Italy*
[5]*The Observatories of the Carnegie Institute for Science, Santa Barbara Street, Pasadena, CA 91101, USA*
[6]*Max-Planck-Institut für extraterrestrische Physik, Postfach 1312, D-85741 Garching bei München, Germany*
[7]*Dipartimento di Fisica e Astronomia, Università degli studi di Bologna, viale Berti Pichat 6/2, I-40127 Bologna, Italy*
[8]*INAF – Osservatorio Astronomico di Roma, Via di Frascati 33, I-00040 Monteporzio Catone, Rome, Italy*
[9]*UCO/Lick Observatory, University of California, Santa Cruz, CA 95064, USA*
[10]*IPP – Max-Planck-Institute for Plasma Physics, Boltzmann Strasse 2, D-85748 Garching bei München, Germany*
[11]*Excellence Cluster, Boltzmann Strasse 2, D-85748 Garching bei München, Germany*
[12]*Steward Observatory, University of Arizona, 933 North Cherry Avenue, Tucson, AZ 85721, USA*
[13]*Space Telescope Science Institute, 3700 San Martin Drive, Baltimore, MD 21218, USA*
[14]*INAF – Osservatorio Astronomico di Brera, via E. Bianchi 46, I-23807 Merate, Italy*
[15]*INFN – Sezione di Trieste, via Valerio 2, I-34127 Trieste, Italy*
[16]*Max-Planck-Institut für Astronomie, Königstuhl 17, D-69117 Heidelberg, Germany*
[17]*Kavli Institute for the Physics and Mathematics of the Universe, Todai Institutes for Advanced Study, the University of Tokyo, Kashiwa 277-8583, Japan*
[18]*Physics Department and Yale Center for Astronomy and Astrophysics, Yale University, New Haven, CT 06511, USA*
[19]*Institute for Astronomy, Department of Physics, ETH Zurich, Wolfgang-Pauli-Strasse 16, CH-8093 Zurich, Switzerland*
[20]*California Institute of Technology, MC 105-24, 1200 East California Boulevard, Pasadena, CA 91125, USA*

ABSTRACT

The mid-infrared-to-ultraviolet (0.1–10 μm) spectral energy distribution (SED) shapes of 407 X-ray-selected radio-quiet type 1 active galactic nuclei (AGN) in the wide-field 'Cosmic Evolution Survey' (COSMOS) have been studied for signs of evolution. For a sub-sample of 200 radio-quiet quasars with black hole mass estimates and host galaxy corrections, we studied their mean SEDs as a function of a broad range of redshift, bolometric luminosity, black hole mass and Eddington ratio, and compared them with the Elvis et al. (E94) type 1 AGN mean SED. We found that the mean SEDs in each bin are closely similar to each other, showing no statistical significant evidence of dependence on any of the analysed parameters. We also measured the SED dispersion as a function of these four parameters, and found no significant dependences. The dispersion of the *XMM*-COSMOS SEDs is generally larger than E94 SED dispersion in the ultraviolet, which might be due to the broader 'window function' for COSMOS quasars, and their X-ray-based selection.

Key words: surveys – galaxies: evolution – quasars: general.

1 INTRODUCTION

The physical details of the continuum emission of active galactic nuclei (AGN) remain unsettled after several decades of study. Yet, understanding the continuum emission of AGN, from X-rays to radio, is essential to unlocking the physics of accretion on to

★ E-mail: henghao@post.harvard.edu

supermassive black holes (SMBHs). The continuum in each spectral region can be ascribed to distinct energy generation mechanisms: jets in the radio (see e.g. the review by Harris & Krawczynski 2006), dust in the infrared (IR; McAlary & Rieke 1988; Sanders et al. 1989), accretion discs in the optical–ultraviolet (UV) and soft X-rays (Shakura & Sunyaev 1973; Rees 1984; Czerny & Elvis 1987), and Compton up-scattering by hot coronae in the hard X-rays (e.g. Zamorani et al. 1981; Laor, Netzer & Piran 1990; Haardt & Maraschi 1991; Williams et al. 1992; Zdziarski, Poutanen & Johnson 2000; Kawaguchi, Shimura & Mineshige 2001; Mateos et al. 2005; Mainieri et al. 2007).

Continuum changes with redshift, luminosity or Eddington ratio might be expected. Most SMBH growth occurs during the active 'AGN' phases (the 'Soltan argument'; Soltan 1982), implying that most galaxy bulges went through an AGN phase (e.g. Magorrian et al. 1998). Rapid growth of central SMBHs happens in high-redshift and high-luminosity quasars emitting near the Eddington limit (Barth et al. 2003; Vestergaard 2004; Jiang et al. 2006; Kurk et al. 2007; but see also Steinhardt & Elvis 2010). The space density of X-ray-selected, highly luminous AGN peaks at around $z = 2.5$ and declines at $z > 3$ (Silverman et al. 2005; Brusa et al. 2009; Civano et al. 2011). Low-luminosity AGN are more prevalent at $z < 1$ than higher luminosity ones (Cowie et al. 2003; Fiore et al. 2003; Ueda et al. 2003; Silverman et al. 2005). As the central SMBH is the driver of the emission, one might expect the quasar spectral energy distribution (SED) to evolve as the black hole grows due to accretion.

Many parameters – the black hole mass, the AGN luminosity relative to the host galaxy, the accretion rate, the physical properties of the accretion disc and the properties of the absorbing dust – might affect the shape of the AGN SED (Wilkes 2003). For instance, the optical-to-X-ray spectral index, $[\alpha_{\rm OX} = 0.384\log(F_{\rm 2\,keV}/F_{\rm 2500\,\mathring{A}})]$, correlates with luminosity but not with redshift (e.g. Vignali, Brandt & Schneider 2003a; Steffen et al. 2006; Just et al. 2007; Lusso et al. 2010; Young, Elvis & Risaliti 2010). It is possible that similar dependence of luminosity on the SED shape exists at other wavelengths.

Observations indicate a tight link between SMBH growth and galaxy evolution (e.g. Magorrian et al. 1998; Tremaine et al. 2002; Marconi & Hunt 2003; Menci et al. 2008). Locally, SMBHs appear to reside at the centre of most galaxies and the SMBH masses are tightly correlated with their masses (e.g. Kormendy & Richstone 1995; Marconi & Hunt 2003) and velocity dispersions (i.e. $M_{\rm BH}-\sigma$ relations; Ferrarese & Merritt 2000; Gebhardt et al. 2000; Tremaine et al. 2002). Some evidence for evolution of this relationship has been reported using several methods (e.g. Peng et al. 2006; Shields et al. 2006; Ho 2007; Merloni et al. 2010). This evolution would imply that the feedback of the SMBH to the host galaxy evolves. Similar evolution in the innermost regions (within the torus) is possible too. All of these processes could lead to different SED shapes.

However, no evolution of the AGN SED has yet been demonstrated. There is no convincing evidence for any change of SED with redshift (Brandt et al. 2002; Mathur, Wilkes & Ghosh 2002; Silverman et al. 2002; Vignali et al. 2003b). High-redshift quasars (up to redshift 7) show optical spectra similar to low-redshift quasars from the Sloan Digital Sky Survey (SDSS; Jiang et al. 2007; Mortlock et al. 2011). There is evidence, though, that the SEDs of extremely low-luminosity ($L_{\rm bol} \lesssim 10^{42}\,{\rm erg\,s^{-1}}$) nuclei are remarkably different from those of luminous ($L_{\rm bol} \gtrsim 10^{44}\,{\rm erg\,s^{-1}}$) AGN (Ho 1999, 2008).

So far, the systematic study of the dependence of the SED shape on physical parameters has been limited by difficulty in obtain-ing a large sample size with good multiwavelength coverage. The Cosmic Evolution Survey (COSMOS; Scoville et al. 2007) has the appropriate combination of depth, area and extensive multiwave-length data that allows for a sensitive survey of AGN to address this question.

The COSMOS field has been imaged with *XMM–Newton* for a total of ∼1.5 Ms (Cappelluti et al. 2007, 2009; Hasinger et al. 2007). Optical identifications were made by Brusa et al. (2010) for the entire *XMM*-COSMOS sample. Photometric properties and redshifts were produced for each point source. This extensive data set allows us to make a systematic study of the evolution of the SED shape, which is the main purpose of this paper.

From this complete sample, we extracted a sample of 413 type 1 AGN (broad emission line full width at half-maximum > 2000 km s⁻¹). The type 1 AGN SED sample catalogue is described in detail in Elvis et al. (2012, hereafter Paper I). It includes quasars with redshifts $0.1 \le z \le 4.3$ and magnitudes $16.9 \le i_{\rm AB} \le 24.8$, with 98 per cent of the sources being radio quiet (Hao et al., in preparation). This sample is 20 times larger than the Elvis et al. (1994, hereafter E94) radio-quiet type 1 AGN SED sample, and has full wavelength coverage from radio to X-rays (for a total of 43 photometric bands; Paper I) and high confidence level spec-troscopic redshifts (Lilly et al. 2007, 2009; Schneider et al. 2007; Trump et al. 2009a). The mean SED of the *XMM*-COSMOS type 1 AGN was calculated and compared to previous studies: E94, Richards et al. (2006, hereafter R06), Hopkins, Richards & Hern-quist (2007), Shang et al. (2011) and Paper I (fig. 21). In this figure, we can see, in the near-IR to optical–UV range, that all recent studies have very similar shapes to E94, while the *XMM*-COSMOS mean host-corrected quasar SED has a less prominent 'big blue bump', possibly due to remnant host contributions, not corrected because of the dispersion in the black hole mass and host luminosity scaling relationship itself. In this paper, we compare the Paper I sample with E94 as a representative.

Paper I presented the selection and properties of the *XMM*-COSMOS type 1 AGN sample of 413 quasars (XC413 hereinafter). We used various radio-loud criteria $[R_{\rm L} = \log(f_{\rm 5\,GHz}/f_B) > 1$, Wilkes & Elvis 1987; $q_{24} = \log(f_{\rm 24\,\mu m}/f_{\rm 1.4\,GHz}) < 0$, Appleton et al. 2004; $R_{1.4} = \log(f_{\rm 1.4\,GHz}/f_J)$, in the observed frame; $q_{\rm 24,obs}$, the q_{24} in the observed frame; $R_{\rm uv} = \log(f_{\rm 5\,GHz}/f_{\rm 2500\,\mathring{A}}) > 1$, Stocke et al. 1992; $P_{\rm 5\,GHz} = \log[P_{\rm 5\,GHz}({\rm W\,Hz^{-1}\,sr^{-1}})] > 24$, Goldschmidt et al. 1999; and $R_{\rm X} = \log(\nu L_\nu(5\,{\rm GHz})/L_{\rm X}) > -3$, Terashima & Wilson 2003] to define a radio-loud quasar. We find that the radio-loud fraction is 1.5–4.5 per cent using any criterion, except $R_{\rm uv}$, which is subject to reddening and host contamination issues (Hao et al., in preparation). Using two criteria at the same time, the radio-loud fraction is $\lesssim 8/413 = 2$ per cent. Only six XC413 quasars satisfy all the seven criteria. We define these six quasars in this catalogue as radio loud (Paper I; Hao et al., in preparation). We refer to the radio-quiet sub-sample of XC413 as XCRQ407 hereinafter.

Estimates of black hole mass ($M_{\rm BH}$) for 206 of XC413 have been made by Merloni et al. (2010) and Trump et al. (2009b). Both papers used single-epoch spectra and applied the scaling relations from reverberation mapping found by Vestergaard & Peterson (2006). This method requires high-S/N spectra with the broad emission line not near the ends of the spectra. For the quasars with only zCOSMOS spectra, the black hole mass was estimated only for those with Mg II lines in the spectra (Merloni et al. 2010), using the calibration of McLure & Jarvis (2002). 206 quasars out of XC413 and 203 quasars out of XCRQ407 have black hole mass estimates. Paper I estimated the host galaxy contribution for 203 of these 206

Table 1. Source properties in parameter space.*

XID	z^a	$\log M_{BH}^b$ ($M_\odot$)	$\log L_{bol}^c$ (erg s^{-1})	λ_E^d	$\log L_{all}^e$ (erg s^{-1})	L_{ir}/L_{all}^f (per cent)	L_{opt}/L_{all}^g (per cent)	L_X/L_{all}^h (per cent)	L_{bol}/L_{opt}	$\log L_{bol, hc}^i$ (erg s^{-1})	$L_{bol, hc}/L_{opt, hc}$
1	0.373	8.58	45.36	0.048	45.46	19.2	37.1	5.6	2.11	–	–
2	1.024	8.96	45.82	0.056	46.09	32.5	17.8	27.6	2.98	45.79	3.35
3	0.345	8.66	45.18	0.026	45.39	33.8	24.1	17.2	2.56	45.11	3.44
4	0.132	7.31	44.25	0.068	44.55	40.8	35.5	3.0	1.41	44.19	1.50
5	1.157	–	45.95	–	46.21	34.2	25.2	12.8	2.18	–	–
6	0.360	8.64	44.89	0.014	45.20	31.1	34.7	4.7	1.42	44.74	1.71
7	0.519	8.38	45.21	0.053	45.44	37.6	27.5	17.9	2.13	45.16	2.46
8	0.699	7.96	45.78	0.518	45.97	33.2	32.2	7.3	2.00	45.78	1.98
9	1.459	8.86	45.90	0.088	46.28	40.1	18.4	11.7	2.30	45.89	2.43
...	...	...	...	...	...	...	...	...	...	...	...

[a] The spectroscopic redshifts are from Trump et al. (2009a), Schneider et al. (2007) and Lilly et al. (2007, 2009).
[b] The black hole mass estimates are from Trump et al. (2009b) and Merloni et al. (2010).
[c] Calculated by integrating the rest-frame SED from 1 μm to 40 keV.
[d] $\lambda_E = L_{bol}/L_{Edd}$, details in Section 2.3.
[e] Calculated by integrating the rest-frame SED from 1.4 GHz to 40 keV.
[f] L_{ir} is calculated by integrating the rest-frame SED from 24 to 1 μm.
[g] L_{opt} is calculated by integrating the rest-frame SED from 1 μm to 912 Å.
[h] L_X is calculated by integrating the rest-frame SED from 0.5 to 40 keV.
[i] Calculated by integrating the rest-frame host-corrected SED from 1 μm to 912 Å for 203 quasars in the *XMM*-COSMOS sample.
*A portion of the table is shown here for guidance. The complete table will be available online.

Table 2. Parameter range.

Parameter	XCRQ407			SSRQ200		
	Min	Med	Max	Min	Med	Max
z	0.10	1.57	4.26	0.13	1.50	4.26
$\log(M_{BH}/M_\odot)$	–	–	–	7.18	8.39	9.34
$\log L_{bol}$ (erg s^{-1})	44.01	45.49	46.91	44.25	45.56	46.91
$\log L_{all}$ (erg s^{-1})	44.29	45.71	47.40	44.55	45.77	47.40
L_{ir}/L_{all}	12.7 per cent	33.2 per cent	76.7 per cent	12.7 per cent	33.4 per cent	76.7 per cent
L_{opt}/L_{all}	2.1 per cent	32.0 per cent	60.5 per cent	9.0 per cent	31.8 per cent	58.9 per cent
L_X/L_{all}	0.33 per cent	8.3 per cent	43.9 per cent	0.47 per cent	8.1 per cent	43.9 per cent
L_{bol}/L_{opt}	1.10	1.90	8.30	1.10	1.84	8.30
λ_E	–	–	–	0.008	0.114	2.505
$\log L_{bol, hc}$ (erg s^{-1})	–	–	–	44.19	45.53	46.86
$L_{bol, hc}/L_{opt, hc}$	–	–	–	1.11	1.94	11.48

quasars using the scaling relationship between the black hole mass and host luminosity (Marconi & Hunt 2003) adding an evolutionary term (Bennert et al. 2010, 2011), excluding the three which had oversubtraction problems (the estimated host galaxy luminosity is larger than the observed luminosity). We define this sub-sample (SS) as SS203. In SS203, 200 quasars are radio quiet. We refer to this sub-sample as SSRQ200.

In Paper I, the rest-frame SEDs of XC413 were constructed on a uniform frequency grid ($\Delta \log \nu = 0.02$) from radio to X-rays. As there are limited data in the far-IR (>10 μm in rest frame) and longer wavelengths, and because the UV flux is strongly affected by both variability and strong broad emission lines, we defer the analysis of these regions to a later paper. In this paper, we focus on the SED shape in the optical-to-mid-IR range (0.1–10 μm), while all the plots are shown in the rest-frame 0.1–10 μm range. Note that all the sources discussed in this paper are broad-line AGN with typical luminosity ($\sim 10^{44}$–10^{47} erg s^{-1}), typical black hole mass ($\sim 10^7$–10^9 M$_\odot$) and typical accretion rates (Eddington ratio larger than 0.01; see Section 2.3).

All the wavelengths discussed in this paper are in the rest frame. We adopt the *Wilkinson Microwave Anisotropy Probe* 5-year

cosmology (Komatsu et al. 2009), with $H_0 = 71$ km s^{-1} Mpc^{-1}, $\Omega_M = 0.26$ and $\Omega_\Lambda = 0.74$.

2 PARAMETER SPACE

2.1 Bolometric luminosity

The bolometric luminosity is the total energy per second radiated by the quasar at all wavelengths in all directions. This luminosity is, in principle, simply calculated by directly integrating the rest-frame SED over the whole wavelength range. In practice, this is difficult and observationally expensive. For the sample discussed in this paper, it is possible to approximate the bolometric luminosity with the SEDs available (Paper I).

As described in Paper I, the SEDs are produced by linearly interpolating between the data points in $\log \nu L_\nu$ versus $\log \nu$ space (i.e. connecting the individual points with power laws in linear space). The COSMOS photometry for the XC413 sample is >90 per cent complete from *u* (Canada–France–Hawaii Telescope) to Multiband Imaging Photometer for SIRTF (MIPS) 24 μm, that is the 1.8 dex wide 0.35–24 μm (~ 0.14–10 μm

Table 3. Bolometric corrections for the SSRQ200 sample.[a]

| λ (μm)	log ν (Hz)	All z BC	σ	0.1 < z < 1.2 BC	σ	1.2 < z < 1.5 BC	σ	1.5 < z < 1.8 BC	σ	1.8 < z < 4.3 BC	σ
9.48	13.5	6.69	4.80	6.60	4.11	6.84	4.95	5.76	3.45	7.59	6.23
7.53	13.6	6.25	4.02	6.74	3.97	6.71	4.18	5.45	2.99	6.13	4.76
5.98	13.7	6.26	3.73	6.98	3.96	6.67	3.81	5.57	2.83	5.82	4.11
4.75	13.8	6.33	3.60	7.01	3.80	6.72	3.64	5.74	2.82	5.85	3.98
3.77	13.9	6.41	3.50	6.73	3.34	6.89	3.69	6.00	3.03	6.04	3.90
3.00	14.0	6.25	3.38	6.12	3.20	6.41	3.20	6.19	3.29	6.27	3.88
2.38	14.1	5.80	3.04	5.82	3.21	5.86	2.86	5.32	2.19	6.22	3.74
1.89	14.2	6.02	3.62	6.34	5.05	6.35	3.25	5.37	2.23	6.03	3.41
1.50	14.3	6.80	4.61	7.13	7.16	7.27	3.84	5.98	2.57	6.83	3.55
1.19	14.4	7.49	4.73	7.97	7.16	8.43	4.55	6.60	2.75	6.98	3.01
0.95	14.5	8.62	8.80	9.81	14.01	10.48	9.58	7.25	2.94	6.92	2.89
0.75	14.6	8.32	14.40	11.30	28.08	8.25	4.90	6.83	2.44	6.90	3.30
0.60	14.7	7.54	12.40	10.96	24.12	7.29	3.54	5.70	2.10	6.23	2.86
0.48	14.8	6.40	4.29	7.77	7.07	6.93	3.12	5.41	1.96	5.49	2.71
0.38	14.9	5.43	2.11	5.98	1.89	6.26	2.63	4.90	1.60	4.58	1.73
0.30	15.0	5.02	2.43	5.71	1.89	5.87	3.56	4.54	1.76	3.93	1.38
0.24	15.1	5.31	3.41	6.14	3.24	6.44	5.08	4.55	1.89	4.10	1.79
0.19	15.2	5.58	5.19	6.87	4.79	6.90	8.47	4.64	2.12	3.91	1.74
0.15	15.3	5.33	6.22	7.01	6.54	6.58	9.69	4.03	2.63	3.71	2.13
0.12	15.4	5.72	6.36	7.20	7.75	6.81	9.18	4.74	2.62	4.14	2.49
0.09	15.5	7.28	6.97	8.00	7.57	7.35	8.77	5.83	3.00	7.99	7.20

[a]After host galaxy subtraction.
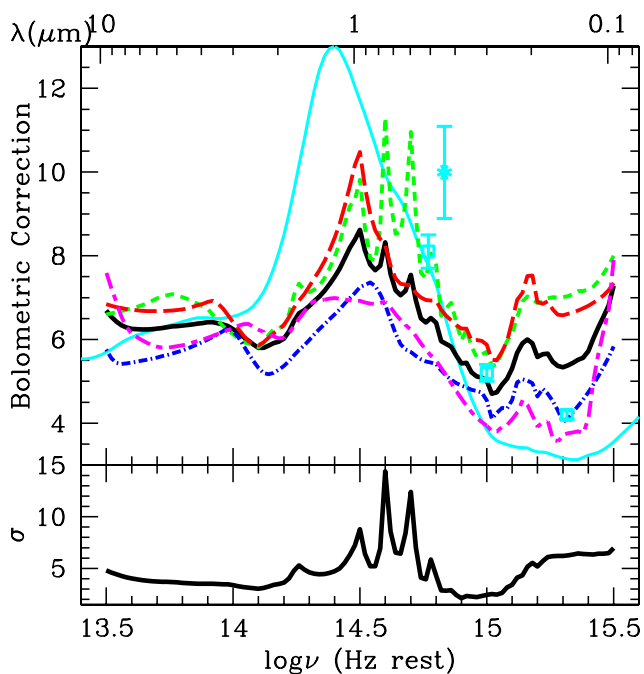
Figure 1. The frequency-dependent bolometric correction for the SSRQ200 sample (black solid). The bolometric corrections in different redshift bins are also shown in the same plot (redshift: 0.1–1.2 = green short dashed line, 50 quasars; 1.2–1.5 = red long dashed line, 50 quasars; 1.5–1.8 = blue dot–dashed line, 51 quasars; and 1.8–4.3 = magenta short–long dashed line, 49 quasars). The cyan solid line shows the bolometric correction for the E94 RQ mean SED. The cyan star point at the *B* band (4400 Å) shows the bolometric correction calculated from Hopkins et al. (2007), assuming $\log L_{bol} = 45.5 \, \mathrm{erg \, s^{-1}}$, which is the median L_{bol} of SSRQ200. The cyan squares show the bolometric correction at 3000 and 5100 Å, respectively from Runnoe et al. (2012). In the bottom panel, we show the dispersion of the bolometric correction for the SSRQ200 sample.

for the typical $z = 1.5$ of XC413) observed-frame interpolation is unproblematic (Paper I). In the mid-IR range, for quasars with 70 or 160 μm detections, we joined the 24 μm data to the longer wavelength points with a power law in $\log \nu f_\nu$ versus $\log \nu$ space; for the others we extrapolated from the rest-frame 24 to 8 μm slope and checked that the extrapolation generally works. As the far-IR-to-radio photometry data are sparse, for each source with a $>3\sigma$ VLA detection, we assumed a power law $f_\nu \propto \nu^{-0.5}$ (e.g. Ivezić 2004) in the rest-frame 1.4 GHz (21 cm) to 100 GHz (3 mm) range. In the 100 GHz (3 mm) to 160 μm part, the SED can be approximated by the red end of the grey body $f_\nu \propto \nu^{3+\beta}/(e^{h\nu/kT} - 1)$, when $h\nu \ll kT$, and $f_\nu \propto \nu^{2+\beta}$ (e.g. Lapi et al. 2011). β is generally chosen in the range 1–2 (Dunne & Eales 2001). We thus choose $\beta = 1$, i.e. we assume a power law $f_\nu \propto \nu^3$ in this wavelength range. We directly linearly interpolate from Lyman break (1216 Å) and 0.5 keV SED in $\log \nu L_\nu$ versus $\log \nu$ space (Laor et al. 1997). In the X-rays, we use the measured photon spectral index ($\Gamma, f_\nu \propto \nu^{(1-\Gamma)}$; Mainieri et al. 2007) and the observed 2 keV luminosity to obtain the SED in the 0.5–40 keV (rest-frame), which is the range of the *XMM* data for XC413.

We used the SEDs from Paper I to calculate two approximations to the bolometric luminosities by integrating the rest-frame SED over different wavelength ranges: (1) from 1 μm to 40 keV as L_{bol}; (2) from 21 cm/1.4 GHz to 40 keV as L_{all}. L_{all} was integrated over all the wavelengths for which we have data.

As the great majority of the XC413 quasars are radio quiet and the photometric coverage from 24 μm to 1.4 GHz is currently sparse (Paper I), using L_{all} requires unwarranted extrapolation. The contribution of the radio emission to the bolometric luminosity is less than 3 per cent even for the radio-loud sources. Most of the far-IR (at $\gtrsim 100$ μm) luminosity is probably due to star-forming activity and not the AGN (Netzer et al. 2007, Mullaney et al. 2012; but see also Ho 2005). From the optical shortward the primary emission is from the innermost region of the quasar (SMBH and accretion disc). The near- and mid-IR continuum is the result of reprocessing shorter
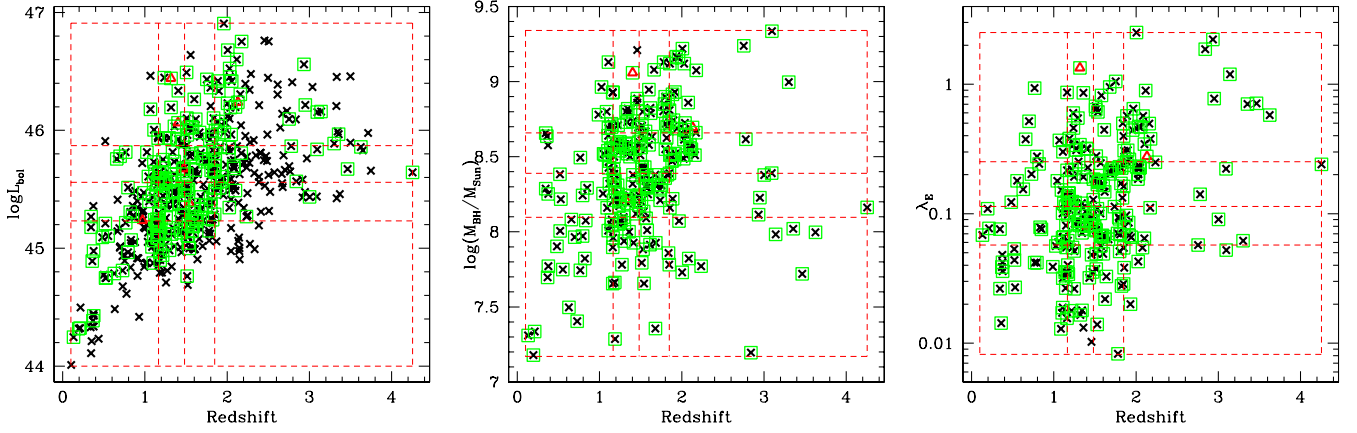
Figure 2. The classification of z, L_{bol}, M_{BH} and $\log\lambda_E$ bins of the *XMM*-COSMOS type 1 AGN sample. The dashed lines show the borders of quartile bins: the z bins ($0.1 \sim 1.2 \sim 1.5 \sim 1.8 \sim 4.3$), L_{bol} bins ($44.0 \sim 45.2 \sim 45.6 \sim 45.9 \sim 46.9$), M_{BH} bins ($7.2 \sim 8.1 \sim 8.4 \sim 8.7 \sim 9.4$) and λ_E bins ($0.008 \sim 0.057 \sim 0.114 \sim 0.252 \sim 2.506$). The black crosses show all the radio-quiet *XMM*-COSMOS type 1 AGN. The red triangles show the six radio-loud quasars. The green squares show the sub-sample SS203.

Table 4. Parameter space bins.

| Bin	Redshift	N		L_{bol}	N		M_{BH}	N	$\log\lambda_E$	N
		XCRQ407	SSRQ200		XCRQ407	SSRQ200		SSRQ200		SSRQ200
1	0.103–1.166	107	50	44.00–45.23	126	50	7.18–8.10	50	0.008–0.057	50
2	1.166–1.483	72	50	45.23–45.56	99	50	8.10–8.39	50	0.057–0.114	50
3	1.483–1.848	84	51	45.56–45.87	93	50	8.39–8.66	50	0.114–0.252	50
4	1.848–4.256	144	49	45.87–46.91	89	50	8.66–9.34	50	0.252–2.506	50
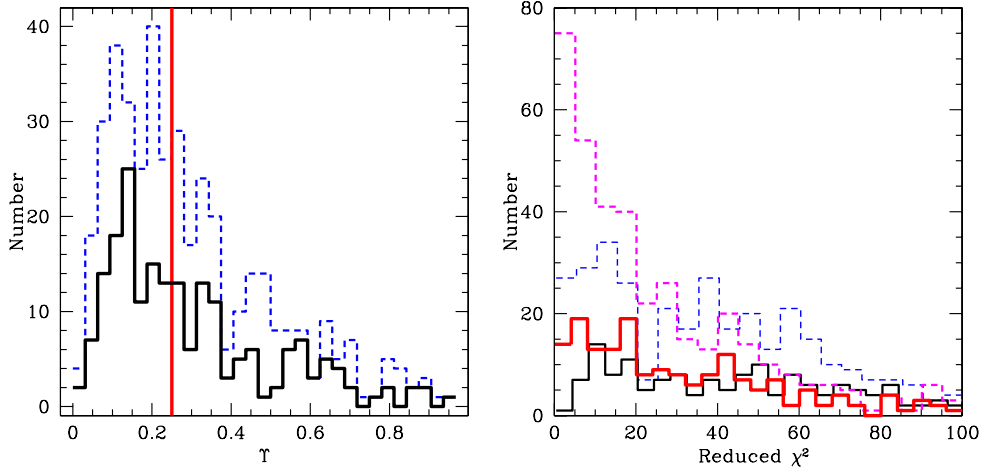
Figure 3. Left: distribution of the variability parameter Υ (Salvato et al. 2009) of the SSRQ200 AGN (black solid line) and XC413 AGN (blue dashed line). The vertical red line divides the sources into variable (>0.25) and not-variable (<0.25). Right: the reduced χ^2 of the SED fitting (see Section 3 for details) both before (black solid line for SSRQ200 and blue dashed line for XC413) and after (red solid line for SSRQ200 and magenta dashed line for XC413) the restriction of the data to the 2004–2007 interval.

wavelength radiation of the quasar by dust (Sanders et al. 1989; Suganuma et al. 2006). The reprocessed dust emission thereby includes reprocessed primary radiation emitted in directions different from our line of sight. In a non-spherical geometry, as is likely present in quasars, this makes us count more radiation than we would in a 4π-averaged calculation. In this sense, we are double-counting the primary emission (e.g. Lusso et al. 2010). Hence, L_{bol} which integrates from 1 μm to 40 keV is a good approximation of the true

bolometric quasar luminosity defined over the entire wavelength range.

We note that directly integrating the SED in the rest frame from 1 μm to 40 keV overestimates the quasar emission as the contribution from the host galaxy is not excluded. In practice, we do not have good estimates of the host contribution. For SSRQ200, we calculated the bolometric luminosity by integrating the host-corrected SED from 1 μm to 912 Å as $L_{bol, hc}$ (last column in Table 1). As
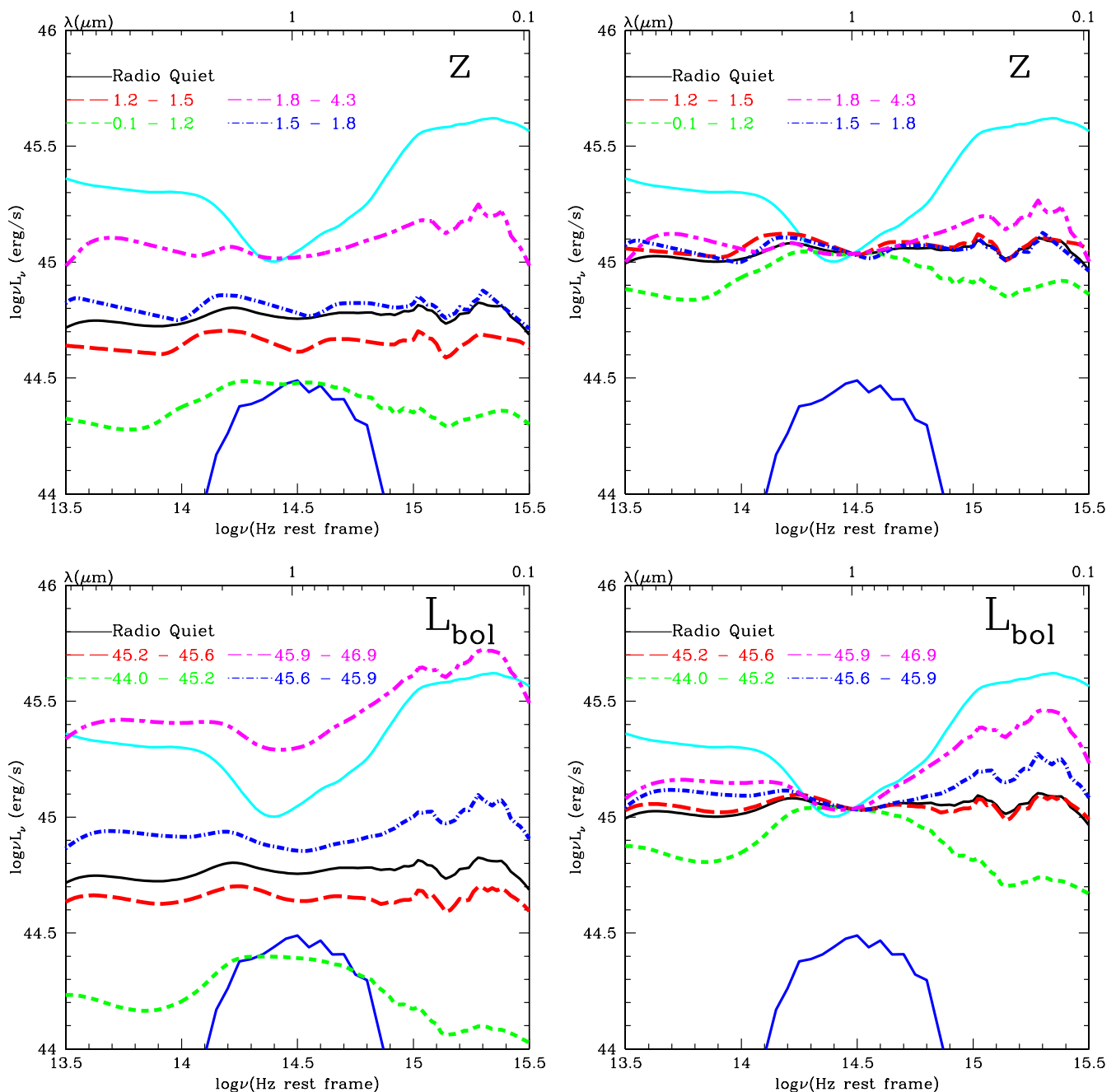
Figure 4. The mean SED for XCRQ407 in bins of z, L_{bol} before (left) and after (right) normalization at 1 μm compared to the E94 mean radio-quiet SED (cyan solid line). The black lines show the mean SED for all the radio-quiet type 1 AGN in the *XMM*-COSMOS sample (XCRQ407). A host galaxy template [an elliptical (5 Gyr), E5, blue solid line] is normalized to L_* from the UKIDSS Ultra Deep Survey (Cirasuolo et al. 2007).

discussed in Paper I, we applied the scaling relationship between the black hole mass and host luminosity reported in Marconi & Hunt (2003), and added an evolutionary term (Bennert et al. 2010, 2011), to estimate the contribution of host galaxy.

We note that L_{bol} will underestimate the total emission for three reasons: (1) excluding the IR to radio emission, (2) excluding the hard X-ray emission, where we do not have data, and (3) ignoring the reddening of the primary emission in the optical/UV. Note that most (if not all) of these factors are not significant underestimate. For example, as we stated above, the contribution of the radio emission

to the bolometric luminosity is less than 3 per cent even for the radio-loud quasars.

To investigate the contribution to bolometric luminosity in different wavelength ranges, we calculated L_{ir} by integrating from 24 to 1 μm, L_{opt} from 1 μm to 912 Å and L_X from 0.5 to 40 keV. The fractions of the luminosity in different wavelength ranges are reported in Table 1 (the full table is available online). Table 2 shows the median values and the ranges for L_{bol}, the fractions in three wavelength ranges, and the median values and the ranges for M_{BH} and Eddington ratio (which will be discussed in Section 2.3). In
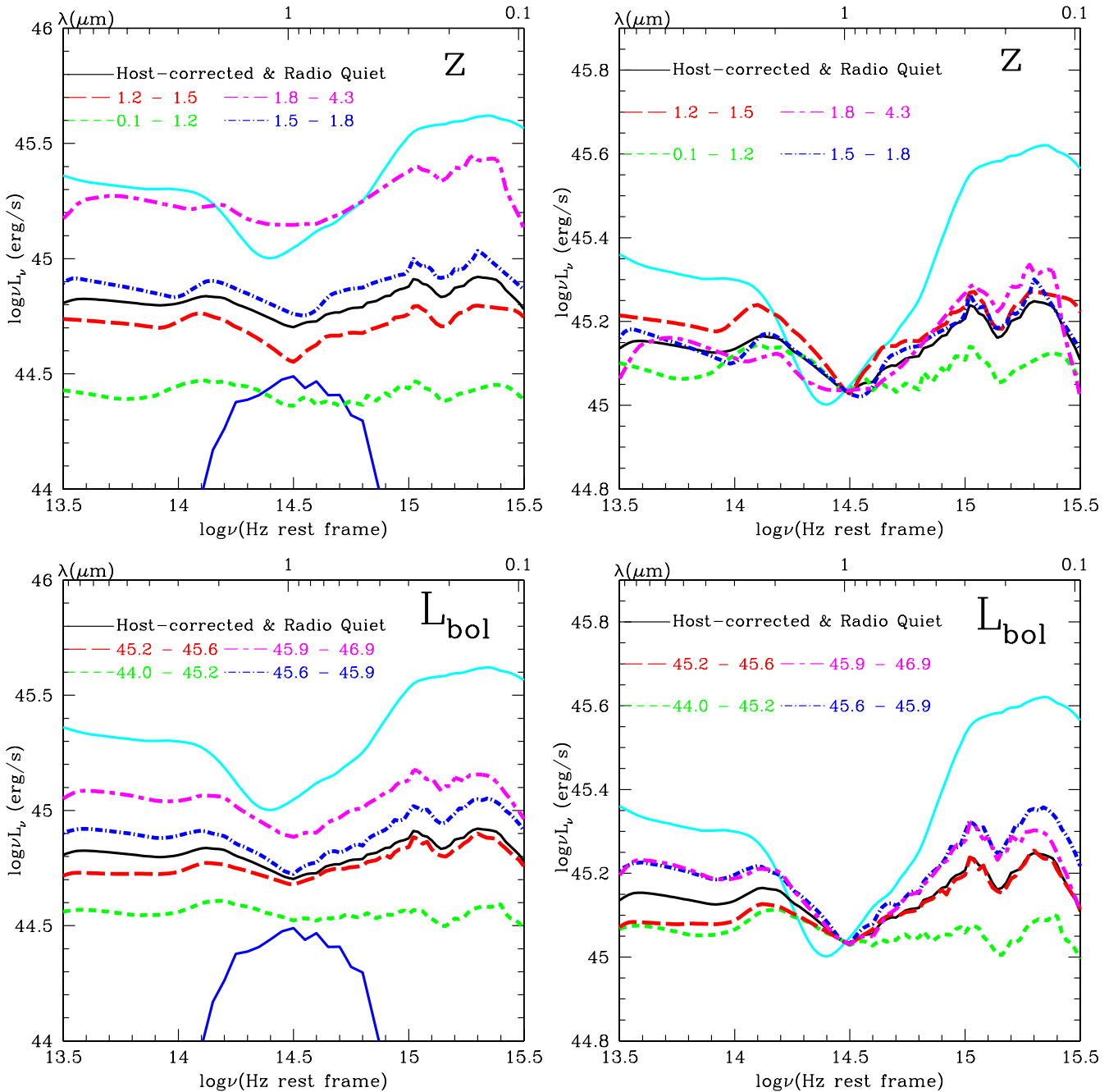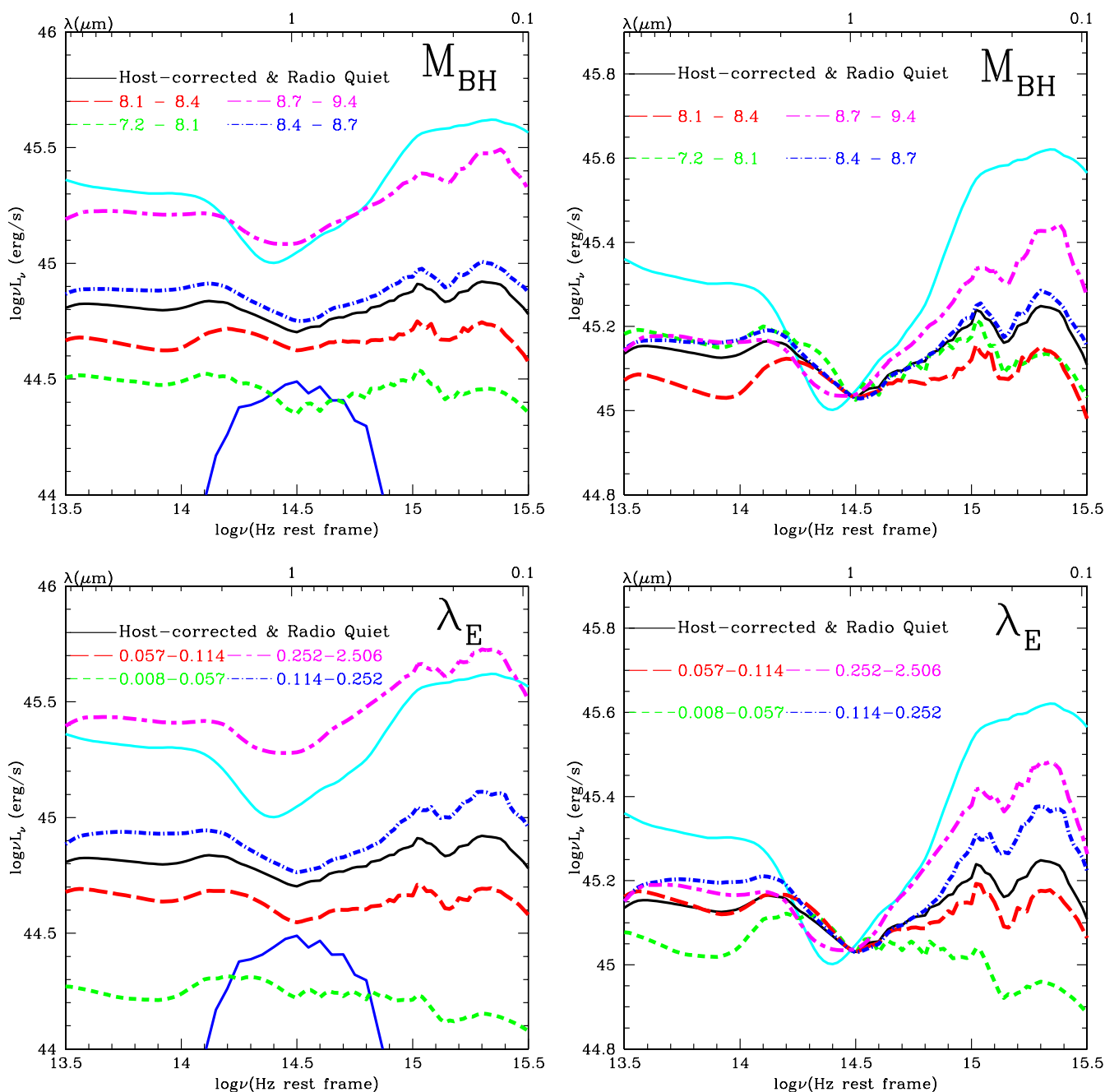
Figure 5. The host-corrected mean SED for SSRQ200 in bins of *z* and L_{bol} compared to the E94 mean radio-quiet SED (cyan solid line) – left: before normalization; right: normalized at 1 μm. The black solid lines show the host-corrected mean SED of all quasars in SSRQ200. A host galaxy template [an elliptical (5 Gyr), blue solid line] is normalized to L_* from the UKIDSS Ultra Deep Survey (Cirasuolo et al. 2007). Note that, to show the difference of the mean SEDs in different bins clearly, we expanded the *y*-axis in all the plots of the right-hand panel.

general, the IR component (1–24 μm) provides an equal or greater contribution compared to the optical/UV 'big blue bump' component (0.1–1 μm). We also calculate the ratio of L_{bol} over L_{opt} as listed in Tables 1 and 2. The mean L_{bol}/L_{opt} is 2.04 ± 0.75 (for XCRQ407) and 2.00 ± 0.71 (for SSRQ200), respectively. The mean $L_{bol, hc}/L_{opt, hc}$ is 2.11 ± 0.91. These values are larger than the ratio for the E94 template (1.86) and for the R06 template (1.61). This is probably caused by the selection effect, that E94 and R06 are optical-selected samples that select more quasars with large optical contribution.

2.2 Bolometric correction

We then calculated the bolometric correction at various frequencies. The bolometric correction ($BC_\nu = L_{bol}/\nu L_\nu$) is the factor which transforms the luminosity in one band to the bolometric luminosity. As the host galaxy contribution is prominent for X-ray-selected quasars, we calculated the frequency-dependent BC in the rest-frame 0.1–10 μm only for SSRQ200 after performing the host correction. The bolometric correction was calculated for a $\Delta \log \nu = 0.02$ grid. The bolometric luminosity used in the

Figure 6. The host-corrected mean SED for SSRQ200 in bins of $M_{\rm BH}$ and $\lambda_{\rm E}$ compared to the E94 mean radio-quiet SED (cyan solid line) – left: before normalization; right: normalized at 1 μm. The black solid lines show the host-corrected mean SED of all quasars in SSRQ200. A host galaxy template [an elliptical (5 Gyr), blue solid line] is normalized to L_* from the UKIDSS Ultra Deep Survey (Cirasuolo et al. 2007). Note that, to show the difference of the mean SEDs in different bins clearly, we expanded the *y*-axis in all the plots of the right-hand panel.

calculation is $L_{\rm bol, hc}$, which is the integration of host-corrected SEDs, listed in the last column of Table 1.

The mean and dispersion of the BC$_\nu$ are listed in Table 3 and shown in Fig. 1, where we also show the mean and dispersion of the BC$_\nu$ for quasars at different redshift bins. The mean BC$_\nu$ curves for different redshift bins are consistent with each other given the large dispersion at each wavelength (Fig. 1). The dispersion is largest at around 1 μm, where the host contribution is the highest, and in the extreme UV, where quasar variability is likely to contribute significantly to the observed dispersion.

For comparison, we plot the E94 mean SED bolometric correction as the cyan solid line in Fig. 1. Hopkins et al. (2007) used a double power law to approximate the *B*-band bolometric correction,

$$\frac{L_{\rm bol}}{L_B} = 6.25 \left(\frac{L_{\rm bol}}{10^{10} \, {\rm L_\odot}} \right)^{-0.37} + 9.00 \left(\frac{L_{\rm bol}}{10^{10} \, {\rm L_\odot}} \right)^{-0.012} .$$

To compare with the bolometric correction we obtained, we use the median value of $L_{\rm bol}$ ($10^{45.5}$ erg s^{-1}) in SSRQ200 to apply to the formula. The *B*-band bolometric correction from Hopkins et al. (2007) is thus 9.99 (cyan star in Fig. 1). More recently, Runnoe,
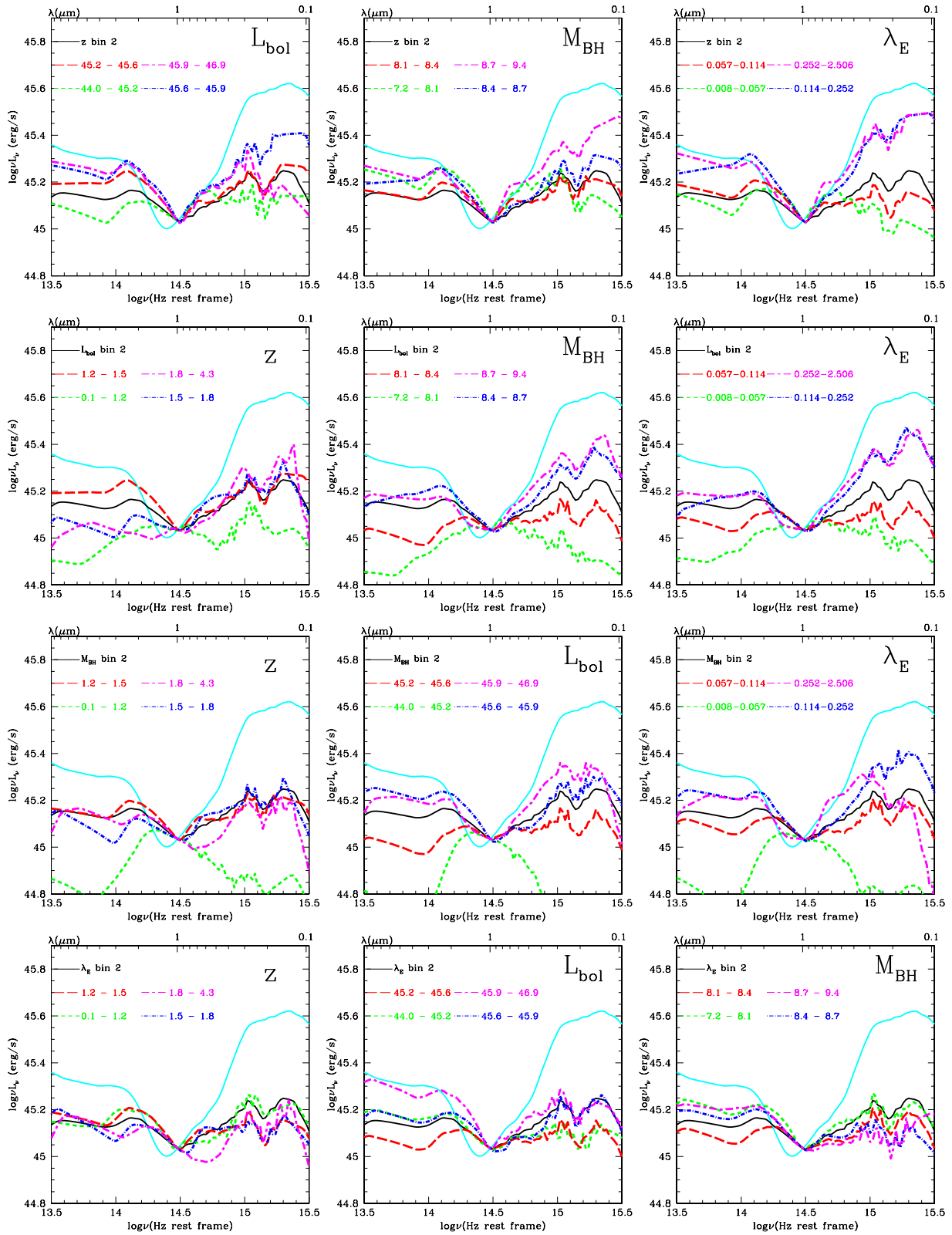
Figure 7. The mean host-subtracted SED normalized at 1 μm compared to the E94 mean radio-quiet SED (cyan solid line). Different rows are for quasars in specific bins: (1) z bin 2 ($1.2 < z < 1.5$); (2) $\log L_{\rm bol}$ bin 2 ($45.2 < \log L_{\rm bol} < 45.6$); (3) $\log(M_{\rm BH}/{\rm M}_{\odot})$ bin 2 ($8.1 < \log(M_{\rm BH}/{\rm M}_{\odot}) < 8.4$); (4) $\log \lambda_{\rm E}$ bin 2 ($0.057 < \lambda_{\rm E} < 0.114$). The symbol on the upper-right corner of each plot shows which sub-bin is considered. The lines are colour coded as in Figs 5 and 6.
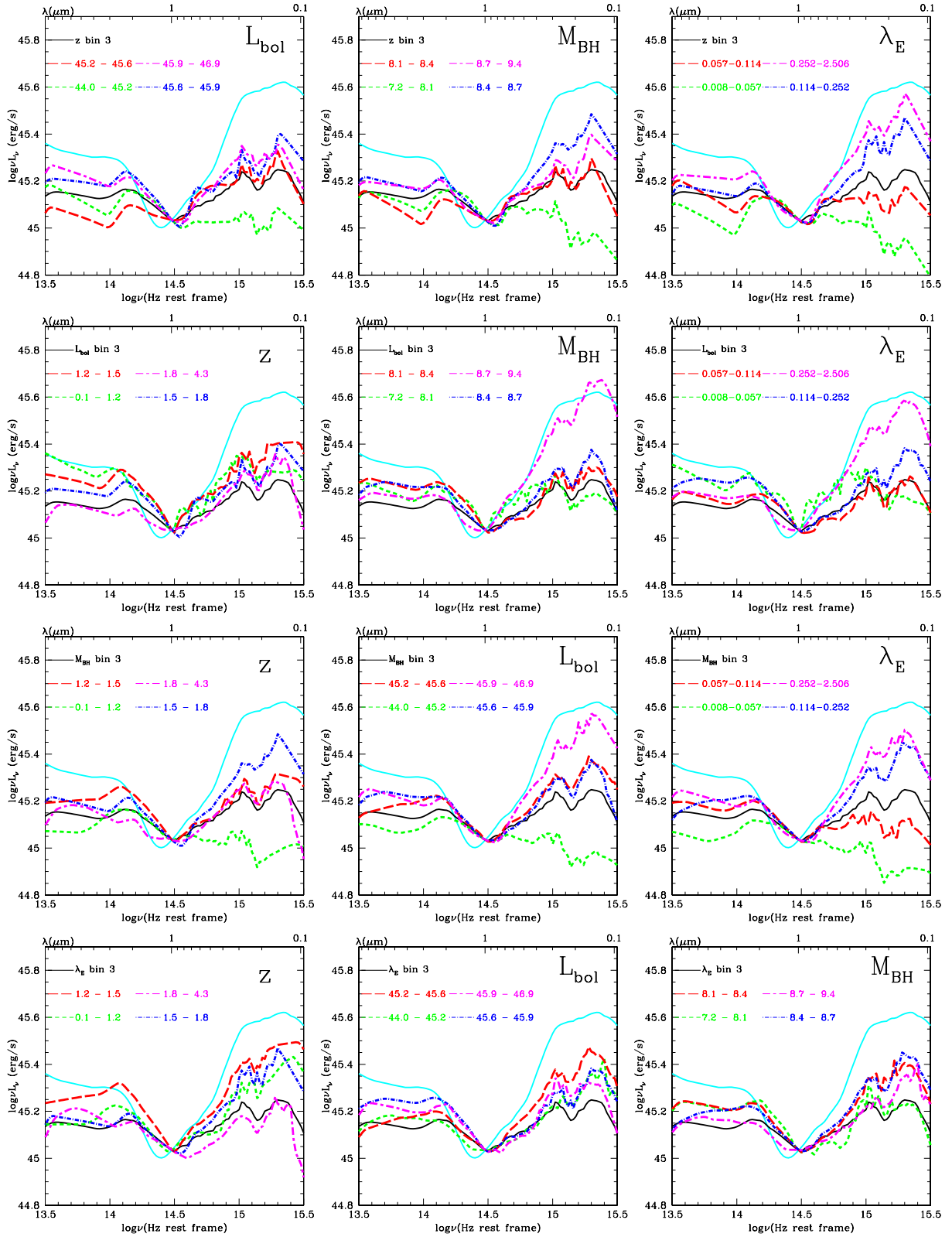
Figure 8. The mean host-subtracted SED normalized at 1 μm compared to the E94 mean radio-quiet SED (red solid line). Different rows are for quasars in specific bins: (1) z bin 3 (1.5 < z < 1.8); (2) $\log L_{bol}$ bin 3 (45.6 < $\log L_{bol}$ < 45.9); (3) $\log(M_{BH}/M_{\odot})$ bin 3 (8.4 < $\log(M_{BH}/M_{\odot})$ < 8.7); (4) $\log \lambda_E$ bin 3 (right half, 0.114 < λ_E < 0.252). The symbol on the upper-right corner of each plot shows which sub-bin is considered. The lines are colour coded as in Figs 5 and 6.

Table 5. Number of SSRQ200 quasars in sub-bins for partial evolution.

Bin	Sub-bin	*z*	L_{bol}	M_{BH}	λ_E
	1		9	11	11
$z(2)$	2		19	15	17
	3		14	13	14
	4		8	11	8
	1		10	11	11
$z(3)$	2		16	15	15
	3		10	15	11
	4		15	10	14
	1	9		6	9
$\log L_{bol}(2)$	2	19		17	19
	3	16		17	13
	4	6		10	9
	1	10		15	10
$\log L_{bol}(3)$	2	14		14	14
	3	10		10	12
	4	16		11	14
	1	11	9		12
$\log M_{BH}(2)$	2	15	17		23
	3	15	14		11
	4	9	10		4
	1	11	15		10
$\log M_{BH}(3)$	2	13	17		10
	3	15	10		19
	4	11	8		11
	1	11	9	13	
$\log \lambda_E(2)$	2	17	19	23	
	3	15	14	10	
	4	7	8	4	
	1	8	11	8	
$\log \lambda_E(3)$	2	14	13	11	
	3	11	12	19	
	4	17	14	12	

Brotherton & Shang (2012) studied the SEDs of 63 bright quasars at low redshift and found a linear bolometric correction of 4.2 ± 0.1, 5.2 ± 0.2 and 8.1 ± 0.4 at 1450, 3000 and 5100 Å, respectively (cyan squares in Fig. 1). These results generally agree with bolometric correction from SSRQ200.

2.3 Eddington ratio

For SS200, the accretion rate relative to the Eddington rate (the Eddington ratio, λ_E) can be calculated given the bolometric luminosities derived in Section 2.1, i.e.

$$\lambda_E = \frac{L_{bol}}{L_{Edd}} = \frac{L_{bol}}{\frac{4\pi G c m_p}{\sigma_e} M_{BH}} = \frac{L_{bol}}{1.26 \times 10^{38} (M_{BH}/M_\odot)}.$$

The black hole mass (M_{BH}) and the corresponding Eddington ratio (λ_E) of the XC413 are listed in Table 1 (full table is available online). The median and ranges of these parameters are reported in Table 2.

2.4 Parameter space classification

The XCRQ407 sample spans a wide range of z, L_{bol}, M_{BH} and λ_E (Table 2, Fig. 2). The redshift range is comparable to that of

Spitzer-SDSS sample (R06), and the luminosity, black hole mass and Eddington ratio ranges are comparable to that of PG quasars (Sikora, Stawarz & Lasota 2007). The size of the XCRQ407 sample is more than double that of previous samples, and is an order of magnitude larger than the E94 sample. This large sample size spanning a wide range of the parameter spaces is useful to understand whether and how the properties of the SMBH affect the SED shape.

XCRQ407 is an X-ray-selected sample and so includes sources with large host galaxy contribution (Paper I). For this reason, we focus on the host-corrected SEDs of the SSRQ200. For comparison, we also study the SEDs of the XCRQ407 before the host correction. The median values and ranges in z, L_{bol}, M_{BH} and λ_E are similar for the two sub-samples (Table 2).

We can now check the SED shape dependence on each physical parameter by dividing the samples into quartiles of quasar z, L_{bol}, M_{BH} and λ_E, as shown by the dashed red lines in Fig. 2. The bin boundaries and number of sources in different bins are given in Table 4. With these divisions, different bins have a similar number of quasars to calculate the mean SED, and therefore the possible statistical differences between different bins are minimized.

3 MEAN QUASAR SED DEPENDENCE ON PHYSICAL PARAMETERS

We can look for trends in the SEDs by checking the mean SED shape diversity in different bins. For each of the z, L_{bol}, M_{BH} and λ_E bins, the mean SEDs are calculated as in Paper I. Briefly we (1) converted the flux densities at each frequency for each object to luminosity, using a Λ cold dark matter concordance cosmology (Komatsu et al. 2009); (2) shifted them to the rest frame for each source; (3) corrected for the small Galactic extinction [$E(B - V) \simeq 0.017$]; (4) limited the variability by restricting the photometry data in use to 2004–2007; (5) corrected for broad emission line contributions, which can be significant in the intermediate-width Subaru bands; (6) linearly interpolated the SED to a uniform frequency grid ($\Delta \log \nu = 0.02$); (7) calculated the mean SED at each $\log \nu$ grid point. To avoid the SED shape being dominated by the few luminous quasars in each bin, we also calculated the mean of the SED after normalizing the SED at 1 μm.

As the COSMOS optical and IR data used here were taken over a 4 yr interval, from 2004 to 2007, and the SDSS data for the field were taken as early as 2001, variability is common in the XC413 sample (Paper I). Salvato et al. (2009) defined a convenient variability parameter Υ (the rms of the magnitude offsets at the sampled epochs) to quantify the variability of the sources. Salvato et al. (2009) found that $\Upsilon > 0.25$ efficiently separates out variable *XMM*-COSMOS sources (including both point-like and extended sources). We plot the Υ histogram in the left-hand panel of Fig. 3 for both the XC413 (blue dashed line) and SSRQ200 (black solid line) samples. Half of the XC413 AGN (199/413) and SSRQ200 AGN (94/200) have $\Upsilon > 0.25$. As in Paper I, we do not use the Salvato et al. (2009) method to correct the SED, to avoid the modification to the SED shape. Alternatively, we restrict the data set to a shorter time period. Using χ^2 fits to the continuum (using quadratic functions to fit the observed data from rest-frame 9000–912 Å), we find that using only the data in the interval from 2004 to 2007 reduces the variability issue (right-hand panel of Fig. 3). The right-hand panel of Fig. 3 shows how the reduced time span improves χ^2 after applying these restrictions.
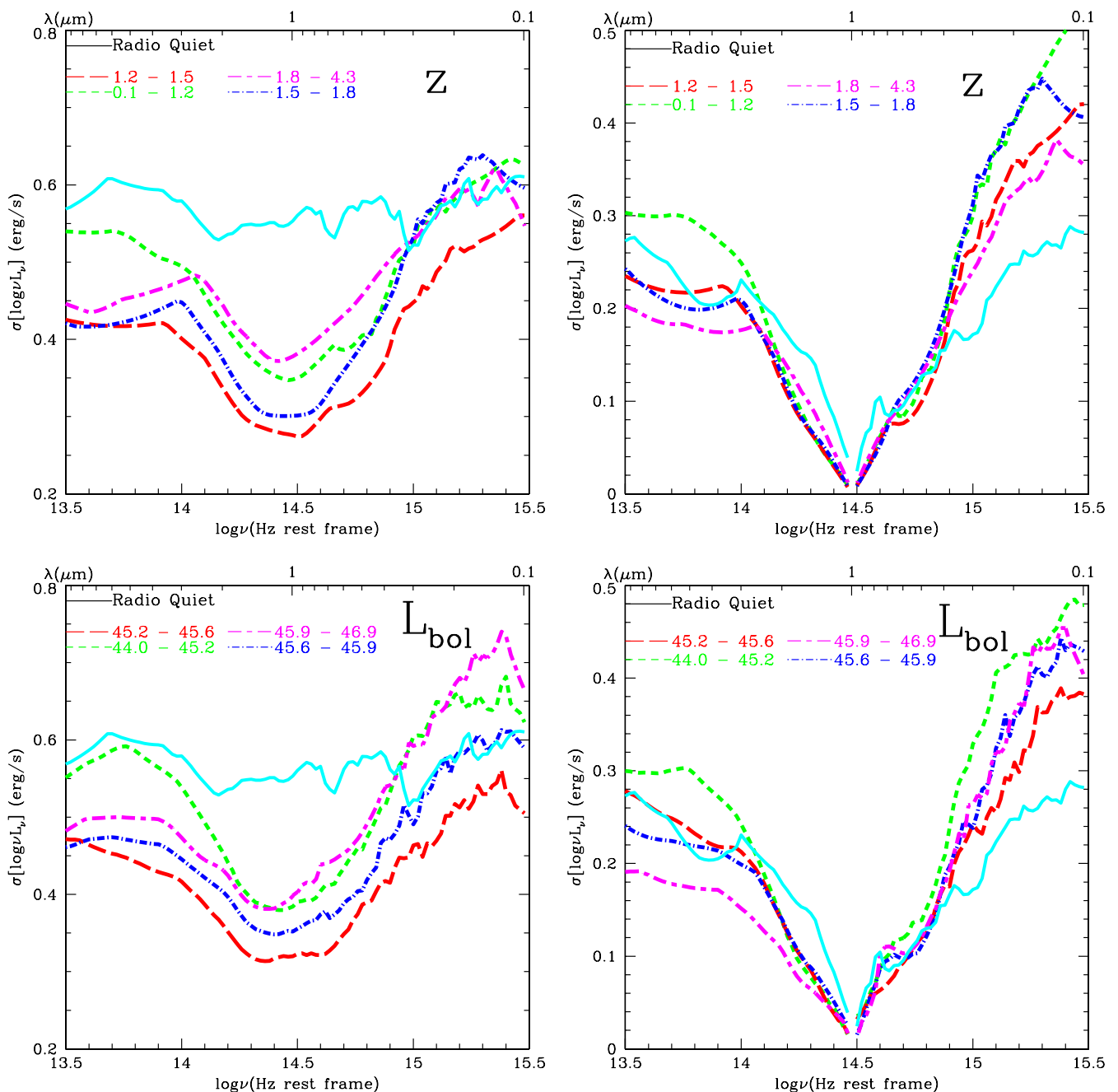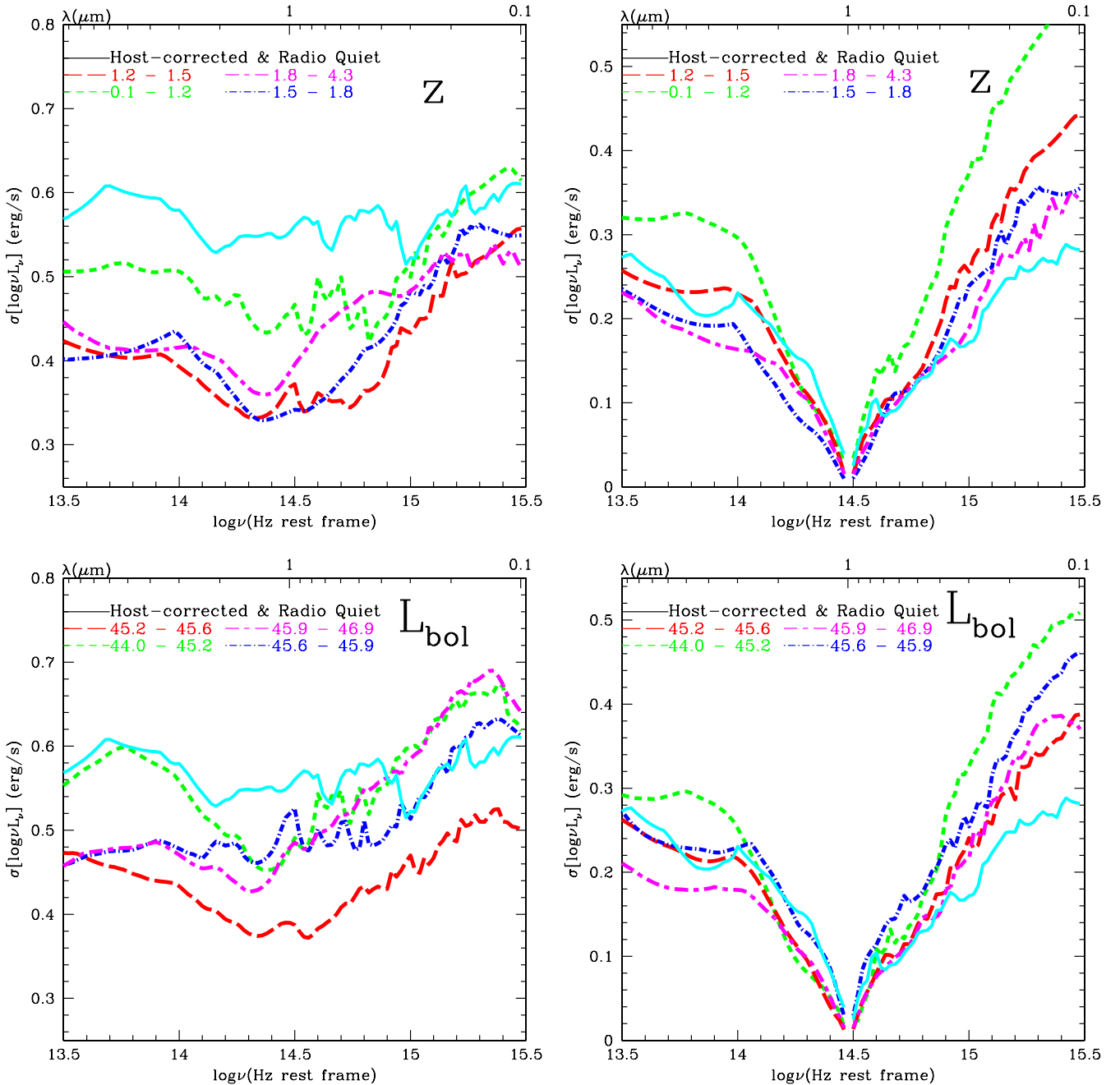
Figure 9. The dispersion of the SEDs for XCRQ407 in bins of z and L_{bol} before (left) and after (right) normalization at 1 μm compared to corresponding E94 radio-quiet SED dispersion (cyan solid curve).

The resulting mean SEDs in different z and L_{bol} bins for XCRQ407 are shown in Fig. 4. For ease of comparison, we also plot the E94 mean SED and a galaxy template from *Spitzer* Wide-area InfraRed Extragalactic Survey (SWIRE; Polletta et al. 2007) normalized to the value of L_* from the The UKIRT Infrared Deep Sky Survey (UKIDSS) Ultra Deep Survey (Cirasuolo et al. 2007, $M_K^* = -23$). The galaxy SED shown is an elliptical galaxy with an age of 5 Gyr (hereafter E5). Different galaxy templates have similar shapes at around 1 μm, so here we just choose E5 as a representative case.

The SEDs in our sample have much less pronounced 1 μm in-flection point than in E94. In Paper I, we concluded that this shape is probably due to the host galaxy contribution. It is clear from

Fig. 4 that for low-z and low-L_{bol} sources the galaxy component around 1 μm strongly affects the shape of the SEDs. Indeed, at higher z and L_{bol}, the 1 μm inflection becomes more obvious, as the quasar component becomes relatively stronger. However, even for high-z and high-L_{bol} sources, the optical big blue bump is not as strong as in E94. This is probably because E94 considered a UV-selected sample which picks out the bluest quasars (Schmidt & Green 1983). The mean SED shapes in the central z and L_{bol} bins are quite similar to the mean SEDs of all the quasars in XCRQ407.

For the SSRQ200 sample, we calculate the mean host-corrected SED for each bin, as shown in Figs 5 and 6. Even with the host correction, the mean SEDs for the low-z and low-L_{bol} sources are

Figure 10. The dispersion of host-subtracted SEDs for SSRQ200 in bins of *z* and *L*$_{bol}$ before (left) and after (right) normalized at 1 μm compared to corresponding E94 radio-quiet SED dispersion (cyan solid curve).

still relatively flat and different from E94. This may be due to insufficient host galaxy correction in some cases because of the scatter in the scaling relationship. The mean SEDs show that the top three bins of *z* and *L*$_{bol}$ have similar shapes, showing no sign of dependence on any of these parameters.

The 1-μm-normalized mean SED shapes of three M_{BH} bins are also similar to each other except for the second bin [8.1 < log ($M_{BH}/M_\odot$) < 8.4]. The optical slopes of the mean SEDs of different λ_E bins increase as λ_E increases, that is the mean SED is redder when the Eddington ratio is smaller. This trend is in agreement with the difference seen in typical quasar with λ_E > 0.01 and

extremely low Eddington ratio AGN with λ_E < 10^{-4} (Ho 2008; Trump et al. 2011).

The *z* bins have the tightest distribution compared to other parameters (e.g. at 3 μm and 3000 Å the difference of the mean SEDs in different bins is 0.1 and 0.15 dex, respectively, smaller than corresponding values of the other parameters). The difference of the mean SEDs in all the bins (except for the lowest bin) of each parameter is less than a factor of 2 even at the IR/UV end.

To check for partial dependences of the SED shape on the physical parameters, we checked the SED shape difference with one parameter when fixing another. In order to have a large enough
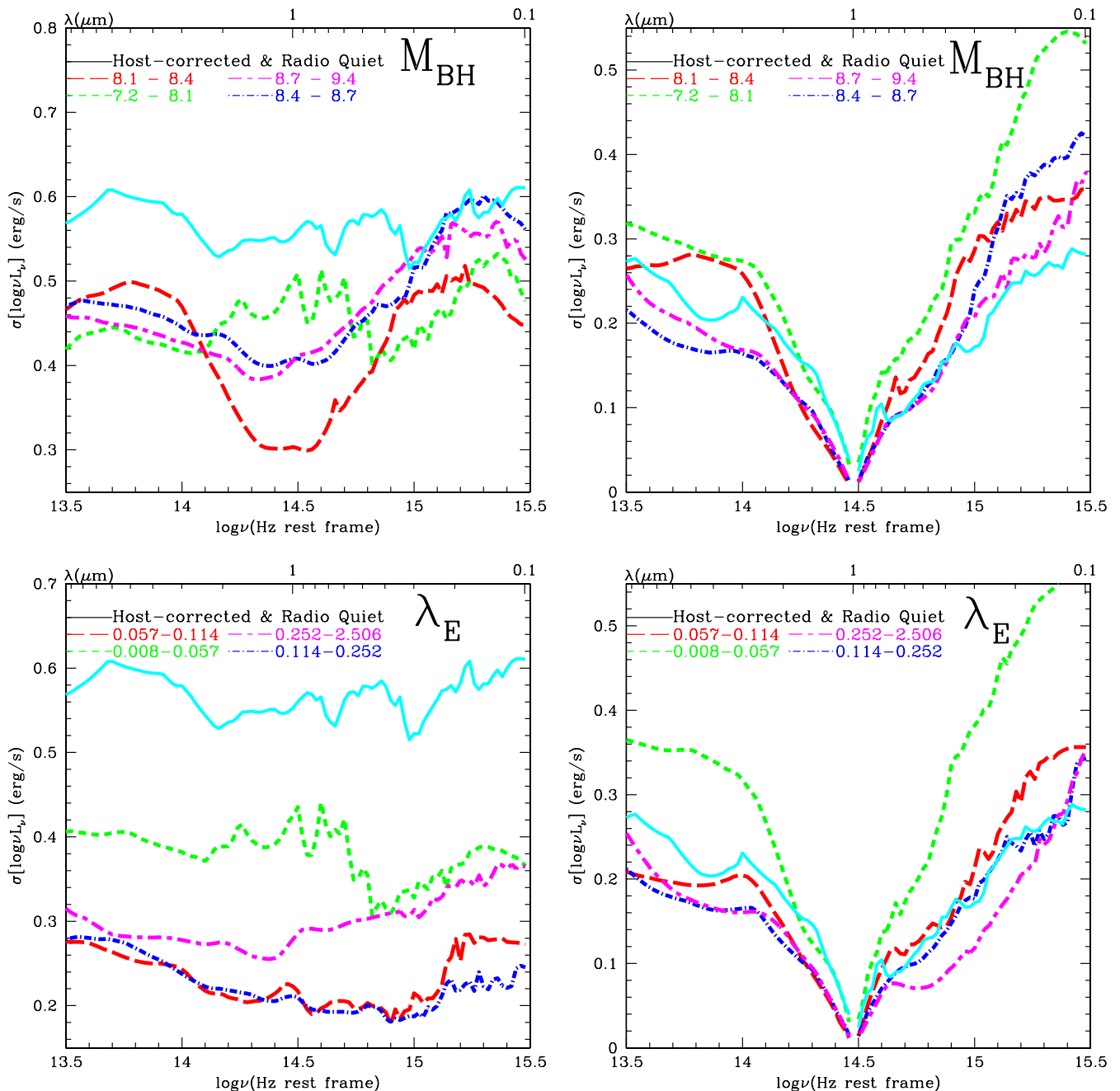
Figure 11. The dispersion of host-subtracted SEDs for SSRQ200 in bins of M_{BH} and λ_E before (left) and after (right) normalized at 1 μm compared to corresponding E94 radio-quiet SED dispersion (cyan solid curve).

number of quasars in the mean SED calculation in each sub-bin, we consider the central two bins (Figs 7 and 8). The number of quasars in each sub-bin is listed in Table 5. As the number of quasars in each sub-bin is relatively small, these mean SEDs are more affected by particular SED shapes. In all these plots, the bottom/first bins are sometimes still affected by the host contribution, and the top/last bins are sometimes affected strongly by several specific SEDs (e.g. hot-dust-poor quasars; Hao et al. 2010, 2011). However, in general, the mean SED shapes in different sub-bins are very similar to each other and to the mean SED in that bin. For instance, when fixing z, the top/last two L_{bol}, M_{BH} or log λ_E sub-bins have a similar mean SED shape, respectively.

As shown in the following section (Section 4), the dispersion of the SED in different bins ranges from 0.3 to 0.6, larger than the difference between the mean SEDs of adjacent bins, and the normalized SED dispersion can be as high as ∼0.5, much larger than the difference between the mean normalized SEDs of adjacent bins (for details, see Section 4). The lack of SED shape dependence on z, L_{bol}, M_{BH} and λ_E we observed in the XCRQ407 and SSRQ200 suggests that neither the emission mechanism nor the accretion disc and torus structure changes systematically or dramatically with these parameters. In other words, a single intrinsic quasar SED in the optical/UV to near-IR range is a meaningful concept. There is still clearly a difference between individual SEDs, for example in

Table 6. Bolometric luminosity dispersion in each bin.

Sample	XCRQ407		SSRQ200			
bin	z	L_{bol}	z	L_{bol}	M_{BH}	λ_E
	$\sigma_{L_{bol}}$	$\sigma_{L_{bol}}$	$\sigma_{L_{bol}}$	$\sigma_{L_{bol}}$	$\sigma_{L_{bol}}$	$\sigma_{L_{bol}}$
1	0.46	0.50	0.45	0.50	0.36	0.26
2	0.38	0.38	0.35	0.38	0.38	0.10
3	0.42	0.43	0.41	0.43	0.43	0.09
4	0.42	0.49	0.39	0.48	0.39	0.25

the normalization due to L_{bol}. However, most of the differences in shapes are caused by different host contributions or reddening in quasars. The SED shape does not show a statistically significant dependence on the parameters we investigated.

4 SED DISPERSION DEPENDENCE ON PHYSICAL PARAMETERS

Even if the mean SEDs show little or no dependence on physical parameters, the SED dispersion may change with them. We checked the SED dispersion in different bins for both the XCRQ407 and SSRQ200 by calculating the dispersion of νL_ν at each frequency in each bin. The dispersion of the SEDs could purely/mostly caused by the luminosity difference among quasars in each bin. In order to distinguish the dispersion caused by different brightness of quasars and the SED shape dispersion, we consider the dispersion of the SEDs before and after normalizing all the SEDs at 1 μm (Figs 9–11). The bolometric luminosity dispersion in each bin is listed in Table 6. From the left-hand panels of Figs 9–11 and Table 6, we can see that majority of the SED dispersion is caused by the luminosity dispersion within bins. For the λ_E bins, the quasar brightness effect is the least. So we will concentrate on the dispersion of the normalized SEDs (right-hand panel of Figs 9–11) to see if there is any SED dispersion dependence on physical parameters. The normalized SED dispersions in different bins at certain specific wavelengths are listed as examples in Table 7.

The resulting dispersions of normalized SEDs in z and L_{bol} bins for XCRQ407 compared to E94 radio-quiet SED dispersion are shown in the right-hand panel of Fig. 9. The *XMM*-COSMOS SEDs generally have a larger dispersion in the optical-to-UV range compared to the E94 radio-quiet sample. This is probably because E94 is biased towards blue quasars, unlike the *XMM*-selected XCRQ407; thus, it does not include quasars with various optical shapes/colours. The 1–10 μm dispersion of XCRQ407 is closely similar to E94, except at ∼2 μm, where it is somewhat lower. The *XMM*-COSMOS SED dispersion is quite similar in the 3 μm to 3000 Å range for different z or L_{bol} bins. The SED dispersions in this range are all below a factor of 2.

For the host-corrected SSRQ200 sample, the dispersion of the SED for each bin is shown in Figs 10 and 11. The SED dispersion in the 3 μm to 3000 Å range is not as tight as the uncorrected sample, implying that extra dispersion induced by the host-correction process depends on z, L_{bol}, M_{BH} or λ_E. The lowest bin for each parameter always has the largest dispersion in most frequency range in all the dispersion plots.

In all these SED dispersion plots, the UV (at ∼0.1 μm) dispersion is generally larger than the near-IR (at ∼10 μm) dispersion. This could mean that the reprocessing of the hot dust component has slightly smoothed the discrepancy of the accretion disc emission. Alternatively, this could be completely caused by the

Table 7. Normalized SED dispersions at certain wavelengths.

Bin	Sub-bin	Wavelength				
		10 μm	3 μm	3000 Å	2500 Å	1000 Å
XCRQ407 z	1	0.30	0.25	0.30	0.36	0.50
	2	0.24	0.20	0.26	0.30	0.42
	3	0.24	0.21	0.31	0.37	0.41
	4	0.20	0.18	0.24	0.28	0.35
XCRQ407 $\log L_{bol}$	1	0.30	0.24	0.33	0.38	0.48
	2	0.28	0.21	0.24	0.26	0.38
	3	0.24	0.20	0.24	0.30	0.43
	4	0.19	0.15	0.26	0.31	0.40
SSRQ200 z	1	0.32	0.30	0.37	0.42	0.57
	2	0.26	0.23	0.26	0.28	0.44
	3	0.24	0.19	0.24	0.26	0.36
	4	0.23	0.16	0.19	0.24	0.34
SSRQ200 $\log L_{bol}$	1	0.29	0.25	0.33	0.37	0.51
	2	0.26	0.22	0.24	0.26	0.39
	3	0.27	0.23	0.25	0.28	0.46
	4	0.21	0.18	0.22	0.27	0.37
SSRQ200 $\log M_{BH}$	1	0.32	0.27	0.33	0.37	0.53
	2	0.26	0.26	0.29	0.31	0.36
	3	0.22	0.16	0.24	0.30	0.42
	4	0.26	0.17	0.21	0.23	0.38
SSRQ200 $\log \lambda_E$	1	0.36	0.32	0.38	0.42	0.56
	2	0.21	0.20	0.21	0.23	0.36
	3	0.21	0.17	0.18	0.21	0.34
	4	0.25	0.16	0.12	0.15	0.35

variability of the quasar which affects the UV SED most, or by reddening.

We can compare the difference between mean SEDs in Section 3 and the SED dispersion discussed above. Before normalization, the SED dispersion is comparable to and slightly larger than the mean SED difference between adjacent bins. As majority of the difference and dispersion is caused by the bolometric luminosity distribution, we will focus our comparison for the normalized SEDs. The normalized SED dispersion can reach up to ∼0.5. At each frequency, the dispersion is much larger than the normalized mean SED difference. We could thus state that the mean SEDs are invariant within 1σ (at most frequencies $>2\sigma$).

5 DISCUSSION AND CONCLUSION

We analysed the dependence of both the mean and dispersion of the SED shapes in the optical–UV to IR range on the parameters z, L_{bol}, M_{BH} and λ_E for the 407 *XMM*-COSMOS radio-quiet type 1 AGN sample. We also calculated the bolometric correction at UV–optical to near-IR for the host-corrected SSRQ200 and in four different redshift bins. The bolometric corrections for different redshift bins are quite similar to each other.

As the *XMM*-COSMOS quasar sample is an X-ray-selected sample, it also includes sources with low nucleus to host contrast. The mean SED of the whole sample is greatly affected by the host galaxy emission for low redshifts and luminosities. Therefore, we mainly studied the mean and dispersion SEDs of a host-corrected sub-sample of 200 radio-quiet quasars, SSRQ200, in four quartile bins of z, L_{bol}, M_{BH} and λ_E. The mean SED shapes in the different bins are quite similar to each other. These SEDs are also generally similar to the E94-like mean SED shape, but they tend to have less pronounced optical-to-UV bump emission than in E94, as E94 is

biased towards blue quasars. Even if we fix one parameter (e.g. redshift), the mean SEDs show no statistical significant evolution with the others.

We checked the dispersion of SEDs in different parameter bins. The near-IR SED dispersion is generally smaller compared to the UV SED dispersion, which might be due to the variability of the quasar that mainly affects UV SED. The SEDs before and after host correction have very similar dispersion in the 3 μm to 3000 Å range for different bins, which implies an invariant intrinsic dispersion of SED shapes in this wavelength range. However, in this wavelength range, the host-corrected SED dispersion is not as tight as the un-corrected sample, probably due to the extra dispersion induced by the scaling relationship which depends on the physical parameters. When we compare the SED dispersion with the difference of the mean SEDs, we could conclude that the mean SED is invariant within 1σ (at most frequencies more than 2σ).

There is no statistical significant dependence of the mean SED with z, L_{bol}, M_{BH} or log λ_E. This result implies that the global quasar structures (the accretion disc and the torus) are invariant with respect to these parameters. Despite the strong expectation that feeding of the AGN and host galaxy is likely to change (e.g. Merloni et al. 2010), as well as the X-ray corona is likely to change (α_{OX} varies with λ_E; e.g. Lusso et al. 2010), the accretion disc and the torus do not seem to depend on this mechanism. Thus, an intrinsic SED in UV–optical to near-IR exists.

The differences among the SEDs show that there might be diversity only at the second order. Host contamination, reddening and quasar variability should lead to a dispersion in the UV and near-IR SEDs. The lack of SED dispersion evolution indicates that these effects themselves do not show much systematic dependence on physical parameters.

All the above conclusions depend on the reliability of the host-correction process. This assumes the scaling relationship between the black hole mass and bulge mass (e.g. Marconi & Hunt 2003) with an evolutionary term (Bennert et al. 2010, 2011). The black hole mass estimates can lead to a dispersion as large as 0.4 (e.g. Vestergaard & Peterson 2006) besides dispersion of the relationship itself. The evolution of this relationship is still under debate (see e.g. Schramm & Silverman 2013). Uncertainties in this correlation might limit our ability to detect SED shape dependence on physical parameters, and it is difficult to estimate the exact amount of dispersion associated with the host-correction process.

A less model-dependent analysis will be described in a following paper (Hao et al. 2013), where we introduce a new mixing diagram to readily distinguish different SED shapes, i.e. galaxy-dominated, quasar-dominated and reddening-dominated SEDs.

So far, we have only studied the SED shape one decade on either side of 1 μm. To study the SED shape evolution in UV or FIR is less easy. The UV is greatly affected by both reddening and variability that are different for different sources. The FIR is greatly affected by host galaxy star formation, which also varies from case to case. We will discuss these two regions of the quasar SED in following papers.

REFERENCES

Appleton P. N. et al., 2004, ApJS, 154, 147
Barth A. J., Martini P., Nelson C. H., Ho L. C., 2003, ApJ, 594, L95
Bennert V. N., Treu T., Woo J.-H., Malkan M. A., Le Bris A., Auger M. W., Gallagher S., Blandford R. D., 2010, ApJ, 708, 1507
Bennert V. N., Auger M. W., Treu T., Woo J.-H., Malkan M. A., 2011, ApJ, 742, 107
Brandt W. N. et al., 2002, ApJ, 569, L5
Brusa M. et al., 2009, ApJ, 693, 8
Brusa M. et al., 2010, ApJ, 716, 348
Cappelluti N. et al., 2007, ApJS, 172, 341
Cappelluti N. et al., 2009, A&A, 497, 635
Cirasuolo M. et al., 2007, MNRAS, 380, 585
Civano F. et al., 2011, ApJ, 741, 91
Cowie L. L., Barger A. J., Bautz M. W., Brandt W. N., Garmire G. P., 2003, ApJ, 584, L57
Czerny B., Elvis M., 1987, ApJ, 321, 305
Dunne L., Eales S. A., 2001, MNRAS, 327, 697
Elvis M. et al., 1994, ApJS, 95, 1 (E94)
Elvis M. et al., 2012, ApJ, 759, 6 (Paper I)
Ferrarese L., Merritt D., 2000, ApJ, 539, L9
Fiore F. et al., 2003, A&A, 409, 79
Gebhardt K. et al., 2000, ApJ, 539, L13
Goldschmidt P., Kukula M. J., Miller L., Dunlop J. S., 1999, ApJ, 511, 612
Haardt F., Maraschi L., 1991, ApJ, 380, L51
Hao H. et al., 2010, ApJ, 724, L59
Hao H., Elvis M., Civano F., Lawrence A., 2011, ApJ, 733, 108
Hao H. et al., 2013, MNRAS, 434, 3104
Harris D. E., Krawczynski H., 2006, ARA&A, 44, 463
Hasinger G. et al., 2007, ApJS, 172, 29
Ho L. C., 1999, ApJ, 516, 672
Ho L. C., 2005, ApJ, 629, 680
Ho L. C., 2007, ApJ, 669, 821
Ho L. C., 2008, ARA&A, 46, 475
Hopkins P., Richards G. T., Hernquist L., 2007, ApJ, 654, 731
Ivezić Ž., 2004, in Mújica R., Maiolino R., eds, Multiwavelength AGN Surveys. World Scientific, Singapore, p. 53
Jiang L. et al., 2006, AJ, 132, 2127
Jiang L., Fan X., Vestergaard M., Kurk J. D., Walter F., Kelly B. C., Strauss M. A., 2007, AJ, 134, 1150
Just D. W., Brandt W. N., Shemmer O., Steffen A. T., Schneider D. P., Chartas G., Garmire G. P., 2007, ApJ, 665, 1004
Kawaguchi T., Shimura T., Mineshige S., 2001, ApJ, 546, 966
Komatsu E. et al., 2009, ApJS, 180, 330
Kormendy J., Richstone D., 1995, ARA&A, 33, 581
Kurk J. D. et al., 2007, ApJ, 669, 32
Laor A., Netzer H., Piran T., 1990, MNRAS, 242, 560
Laor A., Fiore F., Elvis M., Wilkes B. J., Mcdowell J. C., 1997, ApJ, 477, 93
Lapi A. et al., 2011, ApJ, 742, 24
Lilly S. J. et al., 2007, ApJS, 172, 70
Lilly S. J. et al., 2009, ApJS, 184, 218
Lusso E. et al., 2010, A&A, 512, 34
Magorrian J. et al., 1998, AJ, 115, 2285
Mainieri V. et al., 2007, ApJS, 172, 368
Marconi A., Hunt L. K., 2003, ApJ, 589, L21
Mateos S. et al., 2005, A&A, 433, 855
Mathur S., Wilkes B. J., Ghosh H., 2002, ApJ, 570, L5
McAlary C. W., Rieke G. H., 1988, ApJ, 333, 1
McLure R. J., Jarvis M. J., 2002, MNRAS, 337, 109
Menci N., Fiore F., Puccetti S., Cavaliere A., 2008, ApJ, 686, 219
Merloni A. et al., 2010, ApJ, 708, 137

Mortlock D. J. et al., 2011, Nature, 474, 616
Mullaney J. R. et al., 2012, MNRAS, 419, 95
Netzer H. et al., 2007, ApJ, 666, 806
Peng C. Y., Impey C. D., Rix H.-W., Kochanek C. S., Keeton C. R., Falco E. E., Lehár J., McLeod B. A., 2006, ApJ, 649, 616
Polletta M. et al., 2007, ApJ, 663, 81
Rees M. J., 1984, ARA&A, 22, 471
Richards G. T. et al., 2006, ApJS, 166, 470 (R06)
Runnoe J. C., Brotherton M. S., Shang Z., 2012, MNRAS, 422, 478
Salvato M. et al., 2009, ApJ, 690, 1250
Sanders D. B., Phinney E. S., Neugebauer G., Soifer B. T., Matthews K., 1989, ApJ, 347, 29
Schmidt M., Green R. F., 1983, ApJ, 269, 352
Schneider D. P. et al., 2007, AJ, 134, 102
Schramm M., Silverman J. D., 2013, ApJ, 767, 13
Scoville N. Z. et al., 2007, ApJS, 172, 1
Shakura N. I., Sunyaev R. A., 1973, A&A, 24, 337
Shang Z. et al., 2011, ApJS, 196, 2
Shields G. A., Menezes K. L., Massart C. A., Vanden Bout P., 2006, ApJ, 641, 683
Sikora M., Stawarz L., Lasota J. P., 2007, ApJ, 658, 815
Silverman J. D. et al., 2002, ApJ, 569, L1
Silverman J. D. et al., 2005, ApJ, 624, 630
Soltan A., 1982, MNRAS, 200, 115
Steffen A. T., Strateva I., Brandt W. N., Alexander D. M., Koekemoer A. M., Lehmer B. D., Schneider D. P., Vignali C., 2006, AJ, 131, 2826
Steinhardt C. L., Elvis M., 2010, MNRAS, 402, 2637
Stocke J. T., Morris S. L., Weymann R. J., Foltz C. B., 1992, ApJ, 396, 487
Suganuma M. et al., 2006, ApJ, 639, 46
Terashima Y., Wilson A. S., 2003, ApJ, 583, 145
Tremaine S. et al., 2002, ApJ, 574, 740
Trump J. R. et al., 2009a, ApJ, 696, 1195
Trump J. R. et al., 2009b, ApJ, 700, 49
Trump J. R. et al., 2011, ApJ, 733, 60
Ueda Y., Akiyama M., Ohta K., Miyaji T., 2003, ApJ, 598, 886
Vestergaard M., 2004, ApJ, 601, 676
Vestergaard M., Peterson B. M., 2006, ApJ, 641, 689
Vignali C., Brandt W. N., Schneider D. P., 2003a, AJ, 125, 433
Vignali C. et al., 2003b, AJ, 125, 2876
Wilkes B. J., 2003, in Richards G. T., Hall P. B., eds, ASP Conf. Ser. Vol. 311, AGN Physics with the Sloan Digital Sky Survey. Astron. Soc. Pac., San Francisco, p. 37
Wilkes B. J., Elvis M., 1987, ApJ, 323, 243
Williams O. R. et al., 1992, ApJ, 389, 157
Young M., Elvis M., Risaliti G., 2010, AJ, 708, 1388
Zamorani G. et al., 1981, ApJ, 245, 357
Zdziarski A. A., Poutanen J., Johnson W. N., 2000, ApJ, 542, 703

SUPPORTING INFORMATION

Additional Supporting Information may be found in the online version of this article:

Table 1. Source properties in parameter space (http://mnras.oxfordjournals.org/lookup/suppl/doi:10.1093/mnras/stt2274/-/DC1).

Please note: Oxford University Press are not responsible for the content or functionality of any supporting materials supplied by the authors. Any queries (other than missing material) should be directed to the corresponding author for the article.

This paper has been typeset from a TEX/LATEX file prepared by the author.